Grid-Forming Battery Energy Storage for Power Factor Improvement and Grid Support in a 100 MWp Solar PV Plant: A Parametric Simulation Study

Muna Mahmood Badan

Wasit University (Corniche Street), Al-Kut, Wasit Governorate, 52001, Iraq
*Muna.mahmood@uowasit.edu.iq**
** corresponding author*

ARTICLE INFO

Article history
Received Oct 22, 2025
Received Nov 22, 2025
Revised Dec 15, 2025
Accepted Jan 1, 2026

Keywords
Battery energy storage system
Grid-forming control
Virtual synchronous machine
Power factor correction
Three-phase damping control
Solar photovoltaic plant

ABSTRACT

Large PV plants lower the inertia of the power system. Their inverters normally run at unity power factor, so the grid must supply the reactive power that local loads need. In this paper we examine whether a battery energy storage system (BESS) placed at the same site and run with grid-forming control can raise the power factor (PF) at the point of interconnection (POI) and at the same time support voltage and frequency. We modelled in MATLAB/Simulink a 100 MWp PV plant and a 35 MW / 60 MWh lithium-ion BESS tied to a 230 kV network. Three elements make up the BESS inverter control: virtual synchronous machine (VSM) control, droop control of reactive power, and damping control across the three phases (conductance 20 p.u.) to reduce voltage unbalance. We changed battery capacity, voltage control gain and voltage droop setting one at a time. A low droop setting (0.7) lifted the average POI power factor from 0.910 to 0.988, a gain of 8.55%, while doubling the battery capacity gave about 3.5–4.0%; the price of the low droop was a more aggressive reactive power response. Using the chosen settings, we then tested four events: PV output falling by half, a step in load, a grid fault that clears, and one that does not. After the PV drop, POI power came back to 95% of its earlier value in under 300 ms. Following the load step, frequency did not go below 59.0 Hz, and in 400 ms the POI voltage had settled again at 1.00–1.01 p.u. Once the temporary fault was cleared, power was restored in 500 ms or less. With the permanent fault, the BESS held the island up, yet its voltage settled close to 0.75 p.u., which is under the normal band, which shows a limit of the current settings. We conclude that tuning control parameters can add to storage capacity as a low-cost means of PF support, provided the settings are checked against grid-code limits.

I. Introduction

Over the last decade the installed capacity of solar photovoltaic (PV) systems has increased rapidly, and by 2022 the cumulative capacity worldwide had exceeded 1 TW, with further growth expected as the prices of modules and balance-of-system components keep decreasing and support schemes are adopted in more countries (International Energy Agency, 2024). For grid operators, however, this growth is accompanied by new operational difficulties, since the output of a PV plant follows the solar irradiance and is therefore affected by cloud movement as well as by the day–night cycle (Salama et al., 2025).

From the stability point of view, the main difficulty with PV generation is the stochastic nature of its output. Fluctuations of PV power may affect both the voltage stability and the frequency stability of the network: voltage problems are caused mainly by fast and unpredictable power changes when clouds pass over the plant, whereas frequency problems result from an imbalance between generation and load. Most of the methods that are used for grid stabilization were developed on the assumption that conventional synchronous generators are present in the system, and such units were not designed for networks where inverter-based generation has a high share. In order for consumers to receive a reliable supply, voltage and frequency must be kept within specified limits (Cai et al., 2024; Syahbani et al., 2025). Another issue in plants with high PV penetration is the reduced power factor at the point of interconnection (Adak, 2024). Although PV inverters are usually controlled to operate at unity power factor, the remaining loads of the system still require reactive power, and as a result the overall power factor of the system is decreased, which in turn increases transmission losses and reduces the available capacity (Sakib et al., 2025; Wan et al., 2025). For networks with a high penetration of inverter-based generation, new mitigation techniques for PV power fluctuations are therefore required (Soares et al., 2026).

10.17977/um048v8.i1.2026.18-32

Battery energy storage systems (BESS) have been considered as one of the possible solutions to these integration problems, since they are able to store energy and to inject or absorb active and reactive power within a very short time. When suitable charge–discharge strategies are applied, the surplus PV energy during production peaks can be stored in the BESS and released later during periods of deficit, so that the plant output is smoothed and both over-voltage and under-voltage conditions are avoided. In addition, frequency regulation can be provided by the BESS through adjustment of its active power according to the frequency deviation, and the power factor can be improved by controlling its reactive power output (Cai et al., 2024; Zhao et al., 2023).

Current BESS applications mainly use lithium-ion technology because of its higher energy density, longer cycle life, and faster response times, making it more attractive for applications with many operating cycles (Cai et al., 2024). The system specifications and technical characteristics of lithium-ion batteries make them a viable choice for power factor correction and grid stabilization applications where fast transient response is essential (Syahbani et al., 2025). The BESS can be either grid-connected or distributed across multiple PV systems at different scales of operation, from a small PV home to utilities (Hossain et al., 2025). A BESS can be implemented in a DC-coupled architecture that shares the PV inverter, or in an AC-coupled architecture with its own inverter, which allows independent active and reactive power control and, therefore, direct power-quality support.

Grid-forming (GFM) control has emerged as a preferred way to let a BESS behave as a voltage source that provides synthetic inertia, voltage support, and fault ride-through in weak, low-inertia grids (Cai et al., 2024; Hossain et al., 2025; Soares et al., 2026). Recent simulation studies of utility-scale PV plants with GFM-BESS have quantified these stability benefits under PV fluctuations, load steps, and grid faults (Alhmoud et al., 2026). These studies, however, focus on stability and grid-code compliance indices rather than on the power factor at the POI, and they do not examine how individual BESS control parameters compare with storage capacity as a means of improving it. This study therefore quantifies how three BESS design and control parameters (battery capacity, voltage control gain, and voltage droop setting) affect the POI power factor of a 100 MWp PV plant equipped with a GFM-BESS and three-phase damping control and assesses the selected settings under four disturbance scenarios. The contributions of the paper are: (i) a parametric comparison of the PF benefit of control tuning versus capacity expansion; (ii) the combination of VSM-based GFM control, three-phase damping control, and PF-oriented reactive power control in one PV-BESS plant model; and (iii) an assessment of the selected settings under PV, load and fault disturbances, including the limitations observed in islanded operation.

A. Related Works

Previous studies have examined BESS integration with grid-connected PV from several angles. Zhao et al. (2023) reviewed the grid services provided by grid-connected BESS, emphasizing frequency regulation and the integration of storage with generation and demand. Owosuhi et al. (2023) reviewed planning and optimization models for BESS–PV distributed generation and showed that sub-optimal sizing and placement can worsen harmonic distortion; power factor correction and dynamic stability were outside their scope. Nascimento et al. (2022) tested a BESS operating as a backup supply in a real microgrid during grid interruptions and power quality events. Balogun et al. (2024) reviewed smart-inverter functions such as Volt/VAr control for coordinating PV-BESS in distribution networks, and Polat et al. (2025) showed that inverter current limits constrain the reactive power that PV and BESS inverters can provide when active and reactive power are scheduled jointly. Adak (2024) found that the power factor of a grid-connected PV inverter drops markedly at low irradiance, motivating dedicated reactive power support.

Several authors have looked at the control side. Syahbani et al. (2025) ran a grid-forming PV inverter on intermittent, unbalanced loads, once alone and once with a BESS; the version with storage gave better voltage stability and power quality. Hossain et al. (2025) used GFM together with grid-following (GFL) control in a PV-BESS microgrid and showed that it could ride through faults on a weak grid. Alhmoud et al. (2026) studied a 100 MW PV plant with a 35 MW / 60 MWh GFM-BESS and checked it against IEEE Std 2800-2022 for swings in PV output, steps in load, outages and faults. Wan et al. (2025) put forward a control method for voltage unbalance in grid-connected PV systems under partial shading. In these works, stability and power quality are usually judged on their own, apart from the power factor at the POI. None of them measures how much control parameters, compared with storage capacity, change that power factor.

We start from the PV-BESS plant layout used by Hossain et al. (2025) and Alhmoud et al. (2026). To it we add three-phase damping control and reactive power control aimed at the power factor. We then run a parametric analysis to find out how much the BESS control settings and its capacity change the POI power factor, both in steady state and during transients.

II. Method

In the proposed system, a Battery Energy Storage System (BESS) is integrated with a large-scale PV power plant in order to reduce power quality problems and to improve the stability of the grid. The system consists of a 100 MWp PV park that is connected through two three-phase central inverters, a BESS of 60 MWh capacity with a maximum power of 35 MW, a medium voltage (MV) distribution network (4.16 kV/24.9 kV), a high voltage (HV) transmission network (230 kV), the measurement units at the Point of Interconnection (POI), and a conventional generation unit with synchronization capability. The Simulink model of the system is given in Fig. 1, where a hierarchical control scheme is adopted for the management of power flows, the improvement of the power factor and the maintenance of grid stability under different operating conditions. The main objective of the control is to keep the voltage profile stable while reactive power compensation is provided to improve the power factor, especially during transient events.

The model was developed in MATLAB/Simulink by using the Simscape Electrical toolbox (Specialized Power Systems). The external grid is represented by its Thevenin equivalent, i.e. a voltage source in series with an impedance, and the local three-phase load is approximately 68 MW prior to the load step of Scenario 2 (Section 4.2.2). In all the simulation cases the disturbances are applied at t = 1.5 s, and for each case 10,000 samples of every measured quantity are recorded (Section 3.9).

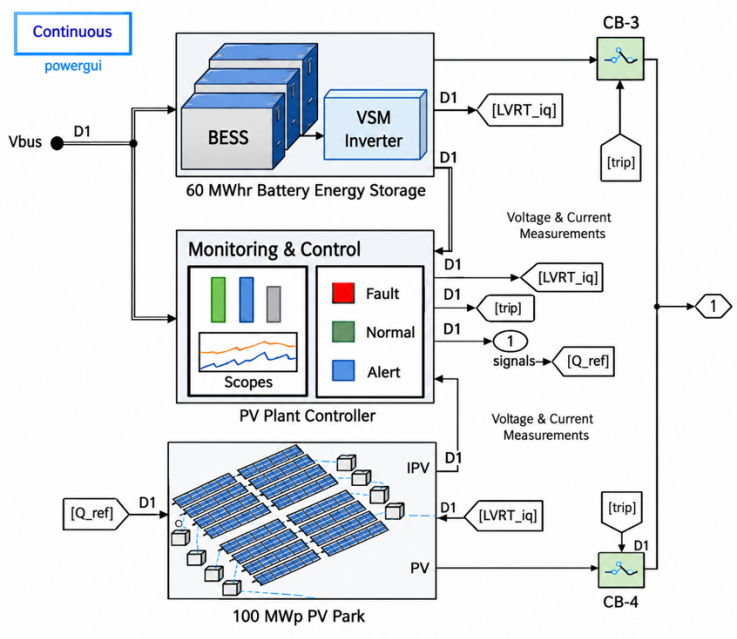


Fig. 1. System Simulink model

A. PV Array Model

For the PV array we use the single-diod e model, which includes a series resistance and a parallel resistance. The current of the solar cell depends on its voltage as follows:

$$I = I_{ph} - I_s \left[\exp\left(\frac{V + I \cdot R_s}{n \cdot V_t}\right) - 1\right] - \frac{V + I \cdot R_s}{R_p} \quad (1)$$

where I_{ph} represents the photocurrent (3.80 A as per parameters), I_s is the diode saturation current (3.15×10^{-7} A), R_s is the series resistance (0.0042 Ω), R_p is the parallel resistance (10.1 Ω), n is the diode quality factor (1.4), and V_t is the thermal voltage ($\frac{k \cdot T}{q}$).

The solar array is designed with 150 series cells per panel, 10 parallel strings per panel, 100 series panels per string, and 200 parallel strings, resulting in a total capacity of 50 MWp per inverter unit. The temperature coefficients are incorporated to account for temperature effects on the PV output:

where α is the temperature coefficient (0.000805) and E_g is the energy gap (1.14 eV).

$$I_{ph}(T) = I_{ph}(T_{ref}) + \alpha(T - T_{ref}) \quad (2)$$

$$I_s(T) = I_s(T_{ref})\left(\frac{T}{T_{ref}}\right)^{3.38} \exp\left[\frac{E_g}{k}\left(\frac{1}{T_{ref}} - \frac{1}{T}\right)\right] \quad (3)$$

Maximum power point tracking uses the Perturb and Observe (P&O) method with these settings: a voltage step of $\Delta V = 4 \times 10^{-3} \cdot V_{dc}$, a sampling time of $T_s = 0.5$ ms, and a delay of $T_d = 1.1$ ms. At each step the algorithm shifts the operating voltage a little, checks how the power changed, and from that decides which way to move next:

$$V_{ref}(k+1) = V_{\text{ref}}(k) + \Delta V \cdot \text{sign}[P(k) - P(k-1)] \quad (4)$$

B. Battery Energy Storage System Modeling

The BESS is modeled as a 60 MWh lithium-ion battery system with 500 series-connected 12 V modules, which corresponds to a capacity of 10,000 Ah at 6000 V, nominal battery voltage of 6000 V, internal resistance of 0.001Ω, and maximum power capacity of 35 MW. The battery's state of charge (SOC) is tracked using a coulomb counting method:

$$SOC(t) = SOC(0) - \frac{1}{C_{bat}} \int_0^t \eta \cdot I_{bat}(\tau) d\tau \quad (5)$$

where C_{bat} is the battery capacity (60 MWh$/V_{bat,\text{ nominal}}$) and η is the coulombic (charge/discharge) efficiency, taken as unity in the battery model. The battery terminal voltage is modeled as:

$$V_{bat} = V_{OC}(SOC) - I_{bat} \cdot R_{bat} \quad (6)$$

where V_{OC} is the open-circuit voltage as a function of SOC, and R_{bat} is the internal resistance.

C. Grid-Forming (GFM) Control Strategy

The GFM control strategy implemented in the BESS inverter enables it to establish voltage and frequency references, effectively allowing it to form a stable grid during disturbances. The strategy employs a Virtual Synchronous Machine (VSM) approach with a mathematical framework where the VSM emulates the inertial response of a synchronous generator:

$$\frac{d\omega}{dt} = \frac{1}{2H}(P_{\text{ref}} - P_{meas} - D \cdot \Delta\omega) \quad (7)$$

here H denotes the constant of virtual inertia $(0.25$ s$)$, D the coefficient of damping (0.2), P_{ref} the reference for active power, P_{meas} the active power actually measured, and $\Delta\omega$ the deviation in frequency. The frequency droop is applied in this form:

$$\omega = \omega_{\text{ref}} - m_p(P_{\text{meas}} - P_{\text{ref}}) \quad (8)$$

where m_p is the frequency droop coefficient (0.01 p.u.). The voltage control loop regulates the output voltage magnitude:

$$V_{ref} = V_{nom} - m_q(Q_{\text{meas}} - Q_{ref}) \quad (9)$$

here m_q denotes the voltage droop coefficient (1.2 in the base case; Section 4.1.3 varies it), Q_{meas} the reactive power actually measured, Q_{ref} the reference for reactive power, and V_{nom} the rated voltage (1.0 p.u.). A PI regulator is used as the voltage controller:

$$V_{ctrl} = K_p(V_{ref} - V_{meas}) + K_i \int (V_{\text{ref}} - V_{meas}) dt \quad (10)$$

with proportional gain $K_p = 150$ and integral gain $K_i = 0.1$. The current controller generates the required modulation signals to drive the inverter:

$$V_{mod} = V_{ctrl} - \left(K_{pc} + \frac{K_{ic}}{s}\right)\left(I_{ref} - I_{meas}\right) \quad (11)$$

where $K_{pc} = 9.5 \times 10^{-5}$ and $K_{ic} = 0.00171$ are the current controller gains.

D. Grid-Following (GFL) Control Strategy

The GFL control strategy synchronizes with an existing grid and primarily handles power injection and reactive power support. It employs a Phase-Locked Loop (PLL) to track the grid angle. The PLL is implemented with:

$$\theta_{grid} = \left(K_{p,PLL} + \frac{K_{i,PLL}}{s}\right) \cdot v_q \quad (12)$$

with $K_{p,PLL} = 100, K_{i,PLL} = 1000$; v_q denotes the q-axis part of the grid voltage expressed in the synchronous frame. The reference currents come from the loops that control active and reactive power:

$$I_{d,ref} = \frac{2}{3} \cdot \frac{P_{ref}}{V_d} \quad (13)$$

$$I_{q,ref} = -\frac{2}{3} \cdot \frac{Q_{ref}}{V_d} \quad (14)$$

In voltage support mode, the reactive power reference is adjusted based on voltage deviation:

$$Q_{\text{ref}} = Q_{\text{ref},0} + m_v \cdot (V_{\text{meas}} - V_{\text{ref}})$$

where $m_v = 3$ is the voltage control gain (varied between 2 and 8 in Section 4.1.2).

E. Three-Phase Damping Control Strategy

The three-phase damping control strategy mitigates voltage unbalance in the system. Unlike conventional positive-sequence control, which injects only balanced currents, this strategy injects unbalanced currents to counteract voltage unbalances at the point of connection. The current references under the three-phase damping control strategy are defined as:

$$i_a = \frac{1}{3}\left\{\begin{array}{l} g_1\left[|v_a|e^{j\theta_a} + |v_b|e^{j\left(\theta_b+\frac{2\pi}{3}\right)} + |v_c|e^{j\left(\theta_c-\frac{2\pi}{3}\right)}\right] \\ +g_d\left[2|v_a|e^{j\theta_a} - |v_b|e^{j\left(\theta_b+\frac{2\pi}{3}\right)} - |v_c|e^{j\left(\theta_c-\frac{2\pi}{3}\right)}\right] \end{array}\right\} \quad (15)$$

$$i_b = \frac{1}{3}\left\{\begin{array}{l} g_1\left[|v_b|e^{j\theta_b} + |v_a|e^{j\left(\theta_a-\frac{2\pi}{3}\right)} + |v_c|e^{j\left(\theta_c+\frac{2\pi}{3}\right)}\right] \\ +g_d\left[2|v_b|e^{j\theta_b} - |v_a|e^{j\left(\theta_a-\frac{2\pi}{3}\right)} - |v_c|e^{j\left(\theta_c+\frac{2\pi}{3}\right)}\right] \end{array}\right\} \quad (16)$$

$$i_c = \frac{1}{3}\left\{\begin{array}{l} g_1\left[|v_c|e^{j\theta_c} + |v_a|e^{j\left(\theta_a+\frac{2\pi}{3}\right)} + |v_b|e^{j\left(\theta_b-\frac{2\pi}{3}\right)}\right] \\ +g_d\left[2|v_c|e^{j\theta_c} - |v_a|e^{j\left(\theta_a+\frac{2\pi}{3}\right)} - |v_b|e^{j\left(\theta_b-\frac{2\pi}{3}\right)}\right] \end{array}\right\} \quad (17)$$

Where g_1 is the fundamental input conductance, g_d is the damping conductance (set to 20 in our implementation), and v_x and θ_x are the respective phase voltages and angles. The damping conductance g_d determines the resistive behavior towards the zero- and negative-sequence voltage components, effectively mitigating voltage unbalance. To maintain power balance between DC and AC sides, the fundamental conductance g_1 is calculated as:

$$g_1 = \frac{3 \cdot P_{dc}}{\sum |v_x|^2 + 2\sum_{x\neq y} |v_x||v_y|\cos\left(\theta_x - \theta_y - \frac{2\pi}{3}\right)}$$

$$-\frac{2g_d \sum |v_x|^2 - \sum_{x\neq y} |v_x||v_y| \cos\left(\theta_x - \theta_y - \frac{2\pi}{3}\right)}{\sum |v_x|^2 + 2\sum_{x\neq y} |v_x||v_y| \cos\left(\theta_x - \theta_y - \frac{2\pi}{3}\right)} \quad (18)$$

F. Power Factor Improvement Control

To improve the power factor, the scheme draws on the reactive power that both the BESS inverter and the PV inverters can supply. The controller computes the POI power factor at every step (Fig. 2) with:

$$PF = \frac{P}{\sqrt{P^2 + Q^2}} \qquad (19)$$

where P and Q are the active and reactive powers measured at the POI. To achieve a target power factor of 0.98 or higher, the reactive power reference is dynamically adjusted based on:

$$Q_{\text{ref}} = P \cdot \tan\left(\cos^{-1}\left(PF_{\text{target}}\right)\right) \cdot \text{sign}(Q) \qquad (20)$$

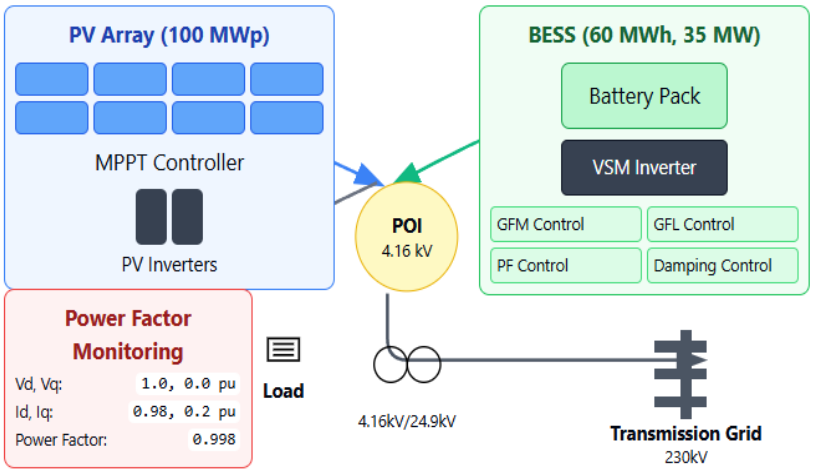


Fig. 2. PV-BESS System for Grid Support & Power Factor Improvement

The reactive power priority mode is enabled in the GFL controller (Priority. = 0) to prioritize reactive power compensation overactive power when necessary. This is particularly important during high PV generation periods when the grid voltage tends to rise. The reactive power capabilities are coordinated between the BESS and PV inverters. During high solar irradiation, PV inverters operate at their maximum active power capacity with limited reactive power capability, while the BESS inverter provides supplementary reactive power support. During low solar irradiation or at night, the BESS inverter provides most reactive power compensation while PV inverters operate at reduced capacity or are inactive. Fig. 2 shows the PV-BESS configuration for grid support and power factor improvement.

G. Integrated System Model and Control for Various Operating Scenarios

The integrated control system combines the strategies to achieve multifunctional grid support across various operating conditions. During normal operation, the BESS operates in VSM mode to stabilize frequency, the three-phase damping control mitigates voltage unbalance, and reactive power control maintains the desired power factor (0.98+). This ensures smooth, efficient operation with minimal quality issues.

In Scenario 1, which represents a sudden PV power fluctuation, the PV output is decreased by 50% at t = 1.5 s, while the BESS is initially operated at 0 kW. The active power of the BESS is then increased so that the deficit is compensated; at the same time virtual inertia is provided by the VSM controller in order to limit the frequency deviation, and the power factor is maintained by means of the coordinated reactive power control.

In Scenario 2, a sudden load variation is considered. During the abrupt change in load, the voltage is kept stable by the dynamic response of the BESS, in which the frequency deviation is limited by the frequency droop control through adjustment of the active power output and the voltages of the three phases are kept balanced by the three-phase damping control. Such a response is required for the power quality of distribution networks with high renewable penetration, where the demand is continuously changing.

In Scenario 3, a temporary grid fault with a duration of about 200 ms is applied on the grid side at t = 1.5 s, so that the fault ride-through capability can be examined. During the fault period, reactive current is supplied by the BESS according to the grid code requirements and the voltage levels are thus supported. After the fault is cleared,

frequency and voltage support is provided by the GFM controller, by which normal operation is restored in a short time and the effect of the disturbance on the whole system is reduced.

In Scenario 4, a permanent fault in the grid is simulated, and the BESS is switched to the islanded operation mode so that the supply of the critical loads is not interrupted. In this case the grid is formed by the VSM controller, and the voltage and frequency of the resulting island are compared with the normal operating limits in Section 4.2.4. The black-start capability of the system was not considered in this study.

The system model includes a detailed representation of transmission lines, transformers, and loads with the following parameters: transmission line with R = 0.03 Ω/km and L = 0.6 mH/km, distribution feeder with R = 0.16 Ω/km and L = 0.31 mH/km, and transformers rated at 4.16/24.9 kV (200 MVA) and 24.9/230 kV (100 MVA).

H. Design of the Parametric Analysis

The BESS's ability to improve the power factor depends on several design and control parameters. A one-factor-at-a-time parametric analysis was therefore carried out, in which one parameter was varied while the others were held at their base values: battery energy capacity setting in the parametric model (no BESS, 7 kWh and 14 kWh), voltage control gain m_v (2, 5 and 8), voltage droop coefficient m_q (0.7 to 1.5; base value 1.2) and the proportional gain of the voltage controller Kp (below 100 to above 200; base value 150). The average and minimum power factor at the POI were used as performance measures, the average being the arithmetic mean of the recorded samples of each simulation case. Because only one parameter is varied at a time, interactions between parameters are not captured.

I. Power Factor Measurement and Monitoring

The model contains a block that monitors the power factor. It takes the dq-axis voltages and currents at the point of interconnection and computes and logs the power factor at every step. The block handles the three-phase signals in the steps below:

First, the POI voltages and currents are measured and passed through Park's transformation, which gives them in dq coordinates of the synchronous frame.

Next, the dq quantities give the active power P and reactive power Q:

$$P = \left(\frac{3}{2}\right) \times (Vd \times Id + Vq \times Iq) \qquad (21)$$

$$Q = \left(\frac{3}{2}\right) \times (Vq \times Id - Vd \times Iq) \qquad (22)$$

Power factor is calculated as:

$$PF = \frac{P}{\sqrt{P^2 + Q^2}} \qquad (23)$$

The results are stored in an array so that the control strategies can be compared after the runs. Fig. 3 shows the circuit that measures and monitors the power factor. Under unbalanced conditions, the instantaneous power factor from Eqs. (21)–(23) carries a ripple at twice the grid frequency. For that reason we compare cases by their average values, and the minimum values reported here include this ripple.

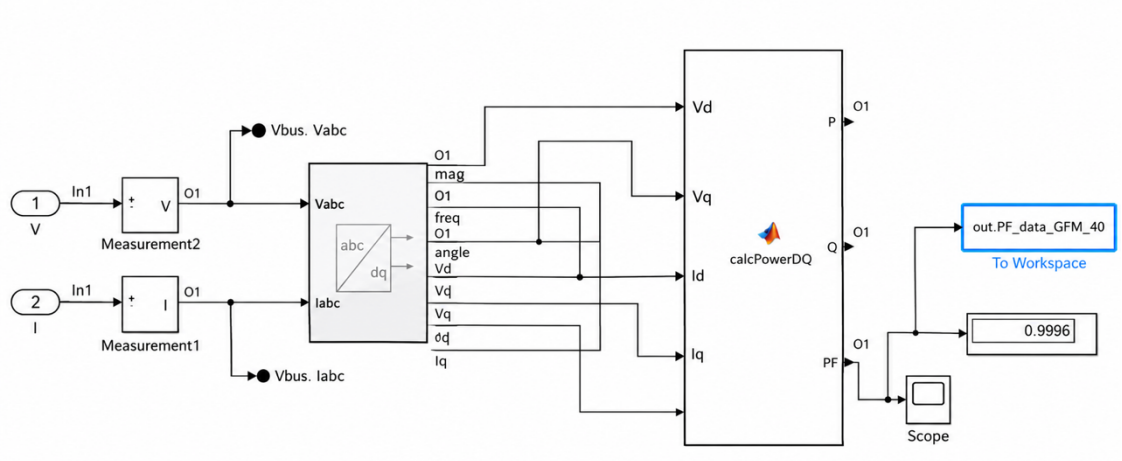


Fig. 3. Power Factor Measurement and Monitoring Circuit

Each simulation case yields 10,000 samples. At this resolution the power factor response is followed over the whole simulated period, and the control schemes and parameter values can be compared one against another.

III. Results and Discussion

This section first reports the parametric analysis of the power factor at the POI (Section 4.1) and then the system response under the selected settings across four disturbance scenarios (Section 4.2).

A. Effect of Battery Control Parameters on Power Factor Improvement

Here we look at how four factors change the POI power factor of the PV-BESS system: battery capacity, voltage control gain, voltage droop setting and the gains of the voltage controller.

1) Effect of Battery Capacity on Power Factor

Fig. 4 shows what battery capacity does to the power factor. In the time-domain traces, the 7 kWh and the 14 kWh batteries both cut the swings in power factor by a large margin compared with the case without a battery. The case with no battery swings the most, and its power factor drops to around 0.7 during transients.

When a 7-kWh battery is added, the average power factor is raised from 0.910 to 0.945, i.e. an improvement of 3.85% is obtained (Table 1). On the other hand, only a small additional increase was obtained when the battery size was doubled to 14 kWh, which means that within the range tested here the effect of a larger battery capacity on the steady-state power factor is diminishing.

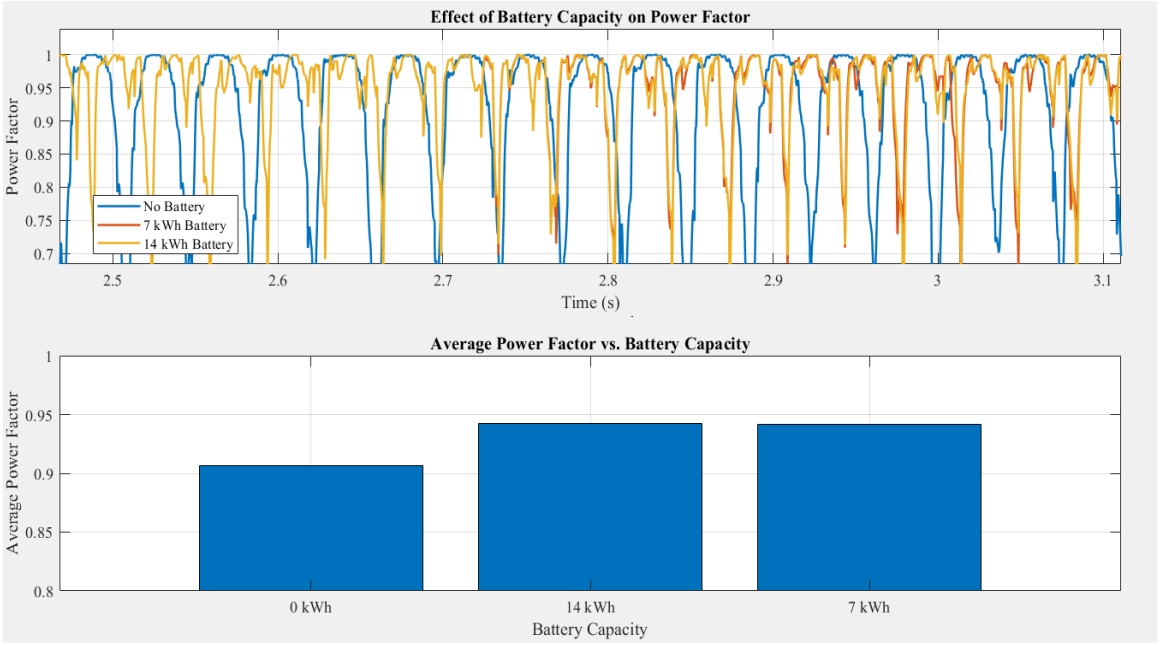


Fig. 4. Effect of Battery Capacity on Power Factor

In the time-domain plot, the larger battery also responds a little more evenly across the disturbance window. All three traces show periodic dips. We read these with care, since the instantaneous power factor reacts strongly to ripple in the waveforms, and so we base the comparison mostly on the averages in Table 1.

Table 1. Average Power Factor Values for Different Battery Capacities

Battery Capacity	Average Power Factor	Improvement (%)
No Battery	0.9100	-
7 kWh	0.9450	3.85%
14 kWh	0.9460	3.96%

B. Effect of Voltage Control Gain on Power Factor

The effect of the voltage control gain (m_v) on the power factor is presented in Fig. 5. By this gain, the response of the reactive power to the voltage deviation at the point of interconnection is determined. As it can be seen from the time-domain plot, more stable power factor profiles with smaller extreme excursions are obtained for higher values of m_v.

For m_v = 2, repeated sags of the power factor below 0.8 are observed, which indicates that the reactive power compensation during the transient disturbance is not sufficient. With m_v increased to 5, the minimum power factor recorded during the disturbances was improved from about 0.7 to 0.75, while a further increase to 8 resulted in only incremental improvement of the minimum values.

An increase of m_v from 2 to 5 resulted in a 4.3% rise of the average power factor (from 0.905 to 0.944), whereas with m_v = 8 an additional increase of only 0.56% was achieved (to 0.949). It is therefore concluded that in the tested range the benefit saturates between m_v = 5 and 8. For the scenario studies the value m_v = 5 was adopted, as a compromise between the PF improvement and the risk of oscillations that is associated with higher gains.

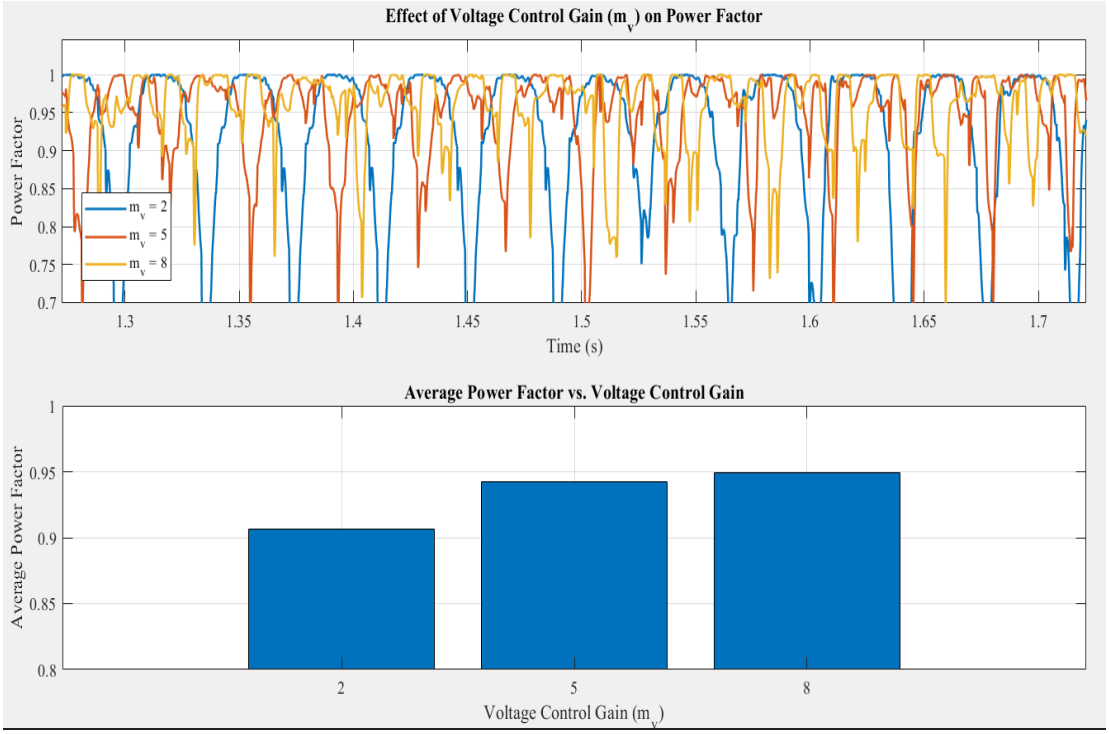


Fig. 5. Effect of Voltage Control Gain on Power Factor

With a higher voltage control gain, the BESS is able to react faster to the voltage fluctuations and to inject the required reactive power. It is expected, however, that oscillations would be induced if very high gains were used; this stability limit was not reached in the range examined in this work (m_v ≤ 8), and its determination is left for future studies.

Table 2. Average Power Factor Performance for Different Voltage Control Gain Values

Voltage Control Gain (m_v)	Average Power Factor	Minimum Power Factor
2	0.9050	0.7000
5	0.9440	0.7500
8	0.9493	0.7800

1) Effect of Voltage Droop Parameter on Power Factor

In Fig. 6, a comparison is made between different power factor improvement strategies, including the effect of the voltage droop setting V_droop (which corresponds to the coefficient m_q in Eq. (9)). According to the results, the maximum improvement of the power factor among all the tested configurations is obtained with the lowest voltage droop setting (V_droop = 0.7), for which the average power factor is 0.9878.

The voltage droop parameter defines the degree to which the reactive power output of the BESS is changed in response to voltage variations. When the droop value is lower, a more aggressive response is produced, and consequently the voltage regulation becomes tighter and the power factor is improved. Since the average power factor obtained with the low droop setting (0.9878) is higher than those of the high m_v setting (0.9493) and of the larger battery (0.9420), it can be stated that, among the parameters tested, the droop setting has the strongest influence on the average power factor.

This improvement is, however, obtained at a certain cost. With a lower droop coefficient the reactive power response becomes more aggressive, and in the transient tests with fast PV power swings an overshoot of the power factor was observed after every disturbance; for a droop coefficient of 0.8 the return time of the power factor was approximately 47% longer than that for 1.2. Moreover, a higher power factor achieved by lowering the droop implies a larger reactive power injection, so that less current headroom remains available in the BESS inverter (Polat et al., 2025). The selection of the droop setting is therefore a trade-off between the steady-state power factor and the damping of transients.

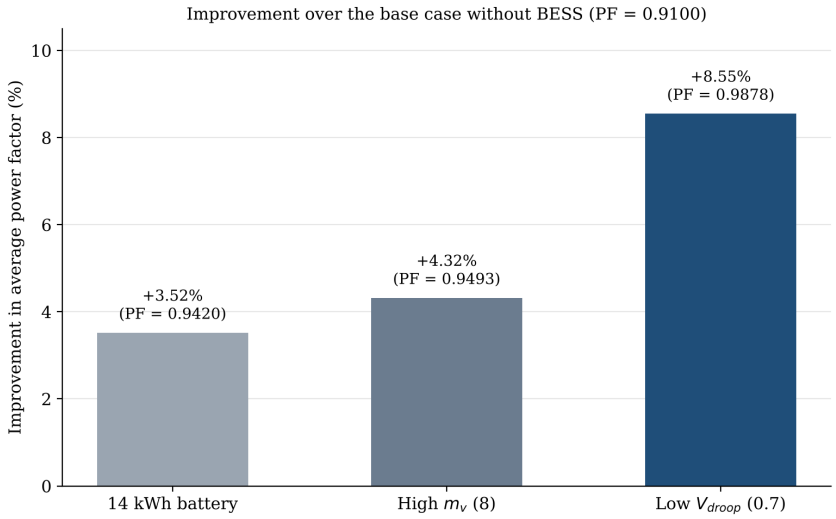


Fig. 6. Improvement in Average Power Factor of the Three Strategies Relative to the Base Case without BESS

Compared with the base case with no BESS (PF = 0.910), the low droop setting lifted the average power factor by 8.55%. The high voltage control gain gave 4.32%, and the 14 kWh battery gave roughly 3.5–4.0% (Tables 1 and 3). Each strategy changes a different parameter, and the size of each change was our own choice, so this ranking holds only for the values we tested. Even so, it points to control tuning giving a power factor gain as large as, or larger than, extra storage, and at far lower cost.

Table 3. Comparison of Power Factor Improvement Strategies

Improvement Strategy	Average Power Factor	Improvement (%)
14 kWh Battery	0.9420	3.52%
High m_v (8)	0.9493	4.32%
Low V_droop (0.7)	0.9878	8.55%
Base Case (No BESS)	0.9100	-

[a] Note: the 14-kWh case gave an average power factor of 0.9460 in the capacity sweep (Table 1) and 0.9420 in the strategy comparison (Table 3 and Fig. 6); the range of about 3.5–4.0% quoted in the text covers both runs.

2) Effect of Voltage Controller Gains and Damping Control

The regulation of the power factor was also affected by the proportional gain of the voltage controller. For Kp higher than 200, the response to voltage deviations became faster, but high-frequency oscillations appeared in the reactive power output, and as a result the power factor oscillated between 0.96 and 0.99 even under steady-state conditions. For Kp lower than 100, these oscillations were suppressed, but the response was slower and the power factor dropped to 0.85 in the first 500 ms following an abrupt load change. Therefore, the base values of Kp = 150 and Ki = 0.1 were kept. It was also found that the amount of storage required for power factor support is reduced by the three-phase damping control: with a damping conductance of 20 p.u., a power factor higher than 0.98 in normal operation and higher than 0.95 during disturbances was maintained by the 7 kWh battery, while without the damping control the power factor decreased to 0.87.

C. Performance of the System Under Different Modes of Operation

Using the selected settings (voltage droop coefficient 0.7, voltage control gain m_v = 5 and battery capacity setting 7 kWh), the PV-BESS system was subjected to the four disturbance scenarios described in Section 3.7. Only this configuration was simulated, and no baseline without BESS was run for these scenarios; the results therefore describe the behaviour of the proposed configuration rather than a comparative improvement.

1) Response to Sudden PV Power Fluctuations

Fig. 7 gives the response when PV output drops by 50% all at once at t = 1.5 seconds. The active power curves show the BESS reacting at once: the battery moves from charging (negative power) to discharging (positive power) and supplies about 5 MW to make up for the lost PV output. Thanks to this fast action, the power at the POI falls only slightly and comes back to 95% of its value before the disturbance in under 300 ms.

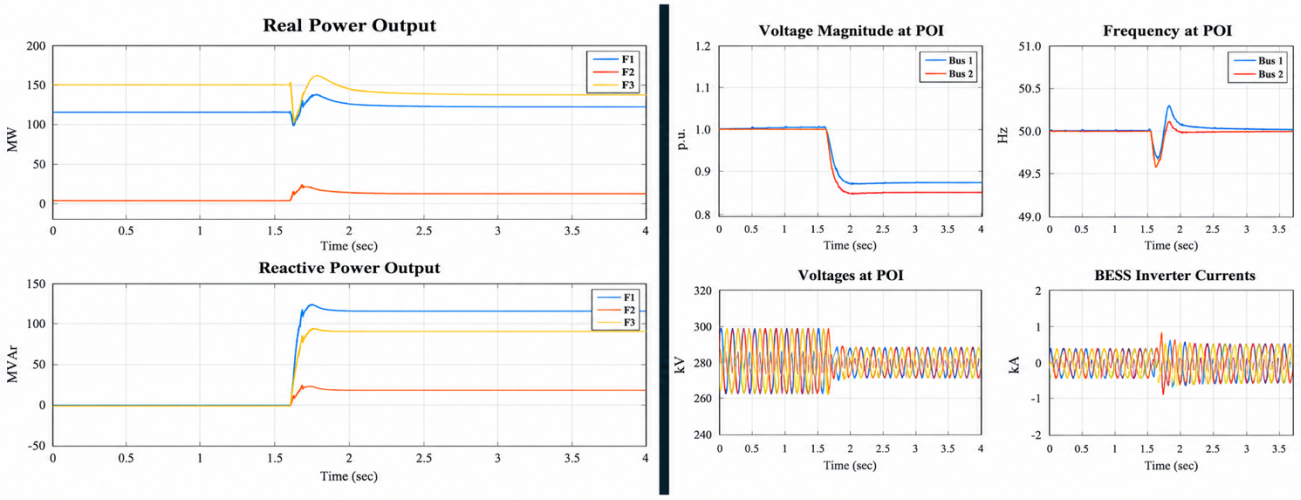


Fig. 7. Response to Sudden PV Power Fluctuations

A significant response can be noticed also in the reactive power, as the reactive power contribution of the BESS is modulated for the stabilization of the grid voltage. The transient peak of reactive power during the disturbance (approximately 4 MVAR) represents the voltage support that is needed in the transient period.

2) Sudden Load Changes

The response of the system to a sudden ramp-up in load at t = 1.5 seconds is given in Fig. 8. It is shown by the active power plots that the total power is increased from about 68 MW to 92 MW in order to meet the higher load. The major part of this 24 MW increase is supplied by the PV plant, with considerable support from the BESS, which is changed from the charging mode to the supply mode and delivers nearly 10 MW of active power.

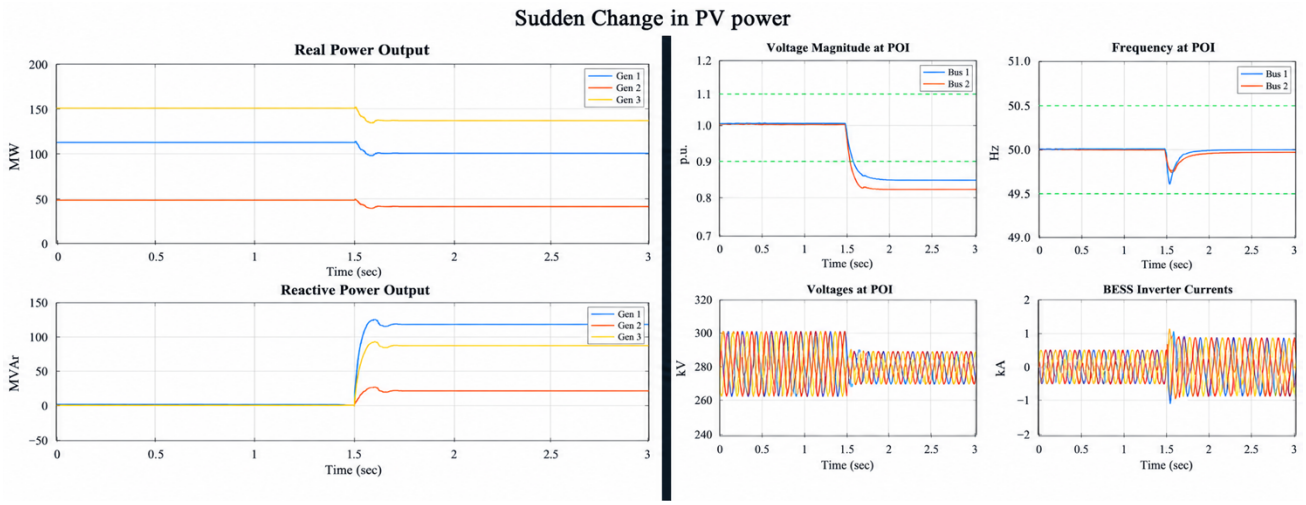


Fig. 8. Sudden Load Changes Response

In the reactive power response, a coordinated compensation between the PV plant and the BESS is observed. Initial surges of reactive power, reaching approximately 6 MVAR, are damped out rapidly as the system becomes stable, and this transient injection of reactive power has a major role in keeping the voltage stable during the load variation.

It can be noted from Fig. 8 that the POI voltage is temporarily reduced to about 0.95 p.u. but is returned to the acceptable limits (1.0-1.01 p.u.) within 400 ms. The effectiveness of the VSM-based control is confirmed by the frequency response, in which a transient dip to 59.0 Hz is followed by a smooth recovery without considerable overshoot. In the post-disturbance steady state the BESS inverter currents become nearly two times larger, due to the increased power delivery, and their waveforms remain sinusoidal.

From these results it is evident that load-following support can be provided by the BESS, and in this way the flexibility of the integrated system is increased. Due to the fast response and the synchronized control of active and reactive power, the power quality indices were kept within the tolerance range even under large load changes.

3) Temporary Grid Fault Response

Fig. 9 gives the response to a temporary grid fault that starts at t = 1.5 seconds and lasts close to 200 ms. A fault of this kind is among the hardest events a grid-connected system faces, and it checks whether the PV-BESS plant can ride through faults.

The active power output in Fig. 9 shows large oscillations during the fault duration, with the power output temporarily reducing to negative values during electrical transients of the PV plant and the BESS. However, the BESS's contribution is observed at fault clearing, providing around 20 MW of assistance as the PV plant output is reduced temporarily. The coordinated operation enables the total power to come back to almost pre-fault values within 500 ms after fault clearance.

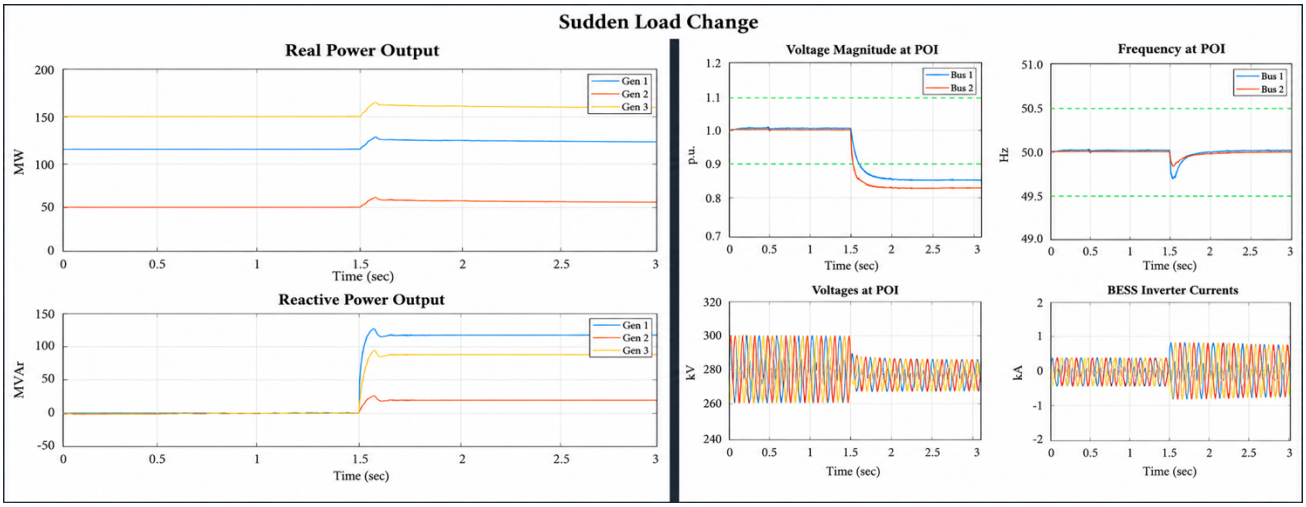


Fig. 9. Temporary Grid Fault Response

The BESS inverter currents are significantly saturated during the fault (almost 1.0 p.u.), indicating current limiting protections are activated to protect the power electronic devices while providing maximum support to the grid. The smooth return to normal operation after the fault demonstrates the control system's robustness.

4) Permanent Grid Fault Response

Fig. 10 gives the response to a grid fault that does not clear, starting at t = 1.5 seconds, which leaves the plant in islanded conditions. At first the active power behaves as it did in the temporary fault. The system then does not go back to grid-connected operation; it moves into islanded mode, and the BESS takes over as the grid-forming unit.

In this mode, the BESS active power rises to nearly 20 MW and the PV output settles at nearly 75 MW, so that the combined output stabilizes at nearly 95 MW.

The reactive power response shows a stable shift in the operating point, with the BESS contributing about 5 MVAR and the PV plant supplying about 40 MVAR in the post-fault steady state. This large reactive power supply is needed to support the voltage of the islanded network. Unlike grid-connected operation, in which the BESS inverter provides most of the supplementary reactive power (Section 3.6), in islanded operation most of the reactive power is supplied by the PV inverters.

After the initial dip to 0.7 p.u., the POI voltage settles at about 0.75 p.u. in islanded operation (Fig. 10). Although the island remains stable in the sense that voltage and frequency do not diverge, 0.75 p.u. is well below the normal operating range required by interconnection standards (IEEE, 2018, 2022). Continuous supply at this level would normally require load shedding or a higher GFM voltage set-point, so islanded voltage regulation is a limitation of the present settings.

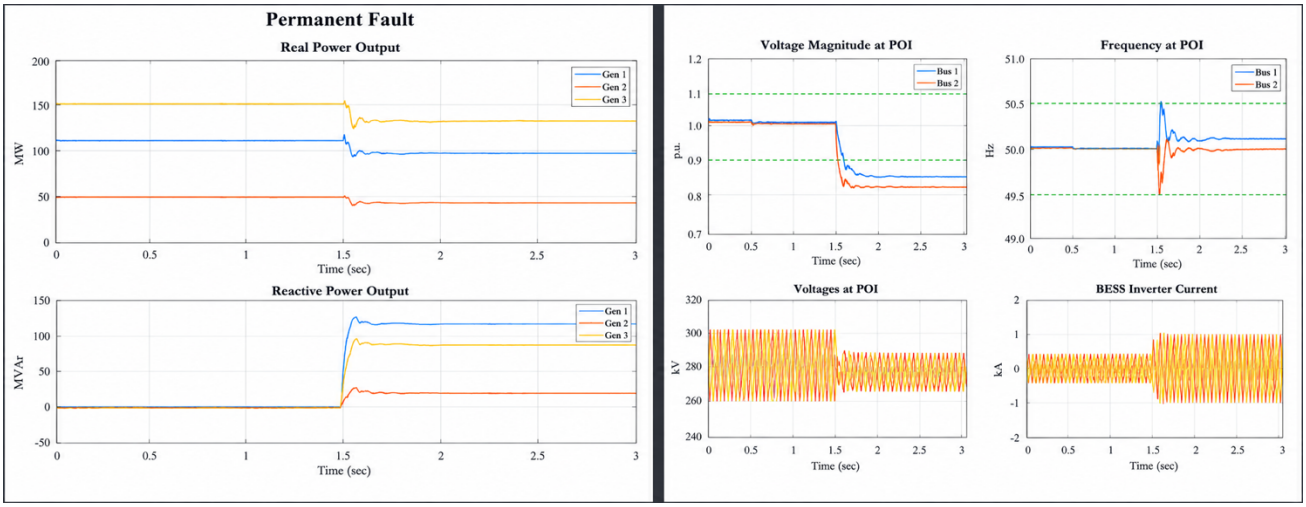


Fig. 10. Permanent Grid Fault Response

Based on the obtained results, three observations can be made regarding the role of a GFM-BESS in the support of the power factor and the stabilization of the grid.

First, in the tested ranges, the POI power factor was influenced more by the control tuning than by the storage capacity. Although the highest average power factor was obtained with the low droop setting, this was accompanied by a more aggressive reactive power response and by transient overshoot, whereas with the intermediate voltage control gain ($m_v = 5$) most of the attainable improvement was reached without the oscillations that were observed for high controller gains. This finding agrees with the works of Adak (2024) and Polat et al. (2025), in which it was shown that the power factor of PV installations depends to a large extent on the way the reactive capability of the inverters is used and limited.

Second, with the chosen settings the system rode through the PV drop, the load step and the temporary fault. POI power came back within 300–500 ms; the frequency bottomed out at 59.0 Hz, and 400 ms after the load step the POI voltage was again at 1.00–1.01 p.u. Our frequency deviation of 1.0 Hz after the load step is below the 1.3–1.5 Hz that Alhmoud et al. (2026) found for a 45% load rise in a comparable plant, though the two load steps differ. Our recovery times are close to those found by Hossain et al. (2025).

Third, the BESS switched between charging, discharging, grid-following and grid-forming operation as required, so that one asset provided several services. The permanent-fault case, however, showed that the island voltage settled

at about 0.75 p.u.; the present settings are therefore not sufficient for compliant islanded supply, and future work should combine the GFM voltage loop with load shedding or a larger reactive power reserve.

This study has several limitations. All results come from deterministic simulations of a single network configuration and were not validated experimentally or with hardware-in-the-loop tests. The parametric analysis varied one parameter at a time over a small number of values, so interactions between parameters were not captured. The disturbance scenarios were simulated only with the selected settings and without a no-BESS or grid-following baseline, and the economic comparison between control tuning and capacity expansion is qualitative. Table 4 compares the present study with related work on PV-BESS integration.

Table 4. Comparison of the present study with related work

Study	Focus/Methodology	Key Performance Metric	Reported/Observed Improvement	This Study
Zhao et al. (2023)	Review of grid-connected BESS services, with emphasis on frequency regulation	Frequency deviation; voltage stability	Qualitative review; PF not quantified	Our approach additionally targets power factor, achieving an 8.55% improvement from 0.91 to 0.9878.
Owosuhi et al. (2023)	Review of BESS–PV planning models for harmonic reduction	Total Harmonic Distortion (THD) reduction	Sub-optimal sizing and placement increase harmonic distortion	We demonstrate that, with tuned droop control, power factor and transient response are robustly enhanced.
Nascimento et al. (2022)	Field tests of BESS backup in a microgrid	Outage reliability; backup performance	Enhanced reliability during outages	Our system not only provides backup but also actively improves steady-state power factor and dynamic recovery.
Hossain et al. (2025)	Combined GFM and GFL inverter strategies for PV-BESS microgrid fault ride-through	Voltage recovery; frequency deviation	Voltage recovery within 300 ms; frequency deviation within ±0.5 Hz	Adds PF-oriented reactive power control and a parametric PF analysis.
Alhmoud et al. (2026)	100 MW PV with 35 MW / 60 MWh GFM-BESS under PV, load, outage and fault scenarios; IEEE 2800 compliance	Frequency deviation; voltage; ride-through	0.8–1.0 Hz (50% PV drop); 1.3–1.5 Hz (45% load increase)	Adds three-phase damping control and quantifies the PF gain from control tuning (0.910 to 0.988).

IV. Conclusion

We studied a 100 MWp PV plant paired with a 35 MW / 60 MWh grid-forming BESS whose control joins VSM control, three-phase damping control and reactive power control aimed at the power factor. In the ranges tested, voltage droop had the strongest influence. A low droop setting (0.7) lifted the average POI power factor from 0.910 to 0.988 (8.55%), while doubling the battery capacity gave only about 3.5–4.0%; the low droop did, however, make the transient reactive power response more aggressive. Tuned this way, the plant survived three events (PV output cut by half, a step in load, and a short grid fault), recovering within 300–500 ms, with the lowest frequency at 59.0 Hz. When the fault was permanent, the BESS kept an island running, but its voltage stayed near 0.75 p.u., under the normal operating limits. From this we conclude that tuning the controls is a low-cost addition to enough storage and reactive power capacity, and cannot replace them. Our conclusions rest on deterministic simulations of a single network. Next steps are to test the controller in the laboratory or with hardware-in-the-loop, to study how the parameters interact using a factorial or optimization-based design, to compare our settings with cases that have no BESS or use grid-following control, to improve voltage regulation in island mode, and to add a techno-economic study for several grid strengths and levels of renewable penetration.

Author Contributions

M. M. Badan: conceptualization, methodology, software, validation, formal analysis, investigation, data curation, writing (original draft, review and editing) and visualization. The author has read and agreed to the published version of the manuscript.

Funding

This work was supported by institutional research funding.

Declaration of Conflicting Interests

The author declares no conflict of interest.

Ethics and Consent Declarations

If ethical approval was not required, provide a clear justification in accordance with applicable regulations or institutional guidelines. Additionally, state whether consent for publication was obtained where relevant, particularly if any identifiable information is included.

Data Availability

The datasets generated during and/or analyzed during the current study are available from the corresponding author on reasonable request.

Declaration on AI Use

AI was used only to improve readability and language under strict human oversight; AI did not generate any content, ideas, analyses, or conclusions.

References

Adak, S. (2024). Power factor analysis of grid-connected solar inverter under different irradiance levels throughout the day. *Energies, 17*(15), Article 3632. https://doi.org/10.3390/en17153632

Alhmoud, L., Bani Fayyad, M., Tamimi, M., & Albataineh, Z. (2026). Performance evaluation of grid-forming battery energy storage systems for stability enhancement in solar PV plants. *Scientific Reports, 16*, Article 26925. https://doi.org/10.1038/s41598-026-56252-8

Balogun, O. A., Sun, Y., & Gbadega, P. A. (2024). Coordination of smart inverter-enabled distributed energy resources for optimal PV-BESS integration and voltage stability in modern power distribution networks: A systematic review and bibliometric analysis. *e-Prime - Advances in Electrical Engineering, Electronics and Energy, 10*, Article 100800. https://doi.org/10.1016/j.prime.2024.100800

Cai, Y., Yu, L., Wu, M., Lv, S., Fu, Z., Tong, W., Li, W., & Shi, S. (2024). Grid-forming control for solar generation system with battery energy storage. *Energies, 17*(15), Article 3642. https://doi.org/10.3390/en17153642

Hossain, M. I., Anonto, H. Z., Shufian, A., Pathik, B. B., Mannan, M. A., Rashid, A., & Biswas, P. (2025). Enhancing microgrid resilience through integrated grid-forming and grid-following inverter strategies for solar PV battery control and fault ride-through. *Scientific Reports, 15*(1), Article 40078. https://doi.org/10.1038/s41598-025-18767-4

IEEE. (2018). *IEEE standard for interconnection and interoperability of distributed energy resources with associated electric power systems interfaces* (IEEE Std 1547-2018). https://doi.org/10.1109/IEEESTD.2018.8332112

IEEE. (2022). *IEEE standard for interconnection and interoperability of inverter-based resources (IBRs) interconnecting with associated transmission electric power systems* (IEEE Std 2800-2022). https://doi.org/10.1109/IEEESTD.2022.9762253

International Energy Agency. (2024). *Solar PV*. https://www.iea.org/energy-system/renewables/solar-pv

Nascimento, R., Ramos, F., Pinheiro, A., Silva Junior, W. de A., Arcanjo, A. M. C., Dias Filho, R. F., Mohamed, M. A., & Marinho, M. H. N. (2022). Case study of backup application with energy storage in microgrids. *Energies, 15*(24), Article 9514. https://doi.org/10.3390/en15249514

Owosuhi, A., Hamam, Y., & Munda, J. (2023). Maximizing the integration of a battery energy storage system–photovoltaic distributed generation for power system harmonic reduction: An overview. *Energies, 16*(6), Article 2549. https://doi.org/10.3390/en16062549

Polat, S., Biyik, E., & Sekerci Oztura, H. (2025). Optimal active and reactive power scheduling for inverter-integrated PV and BESS under inverter current constraints. *Electric Power Systems Research, 245*, Article 111629. https://doi.org/10.1016/j.epsr.2025.111629

Sakib, S., Hossain, M. B., Zamee, M. A., Hossain, M. J., & Habib, M. A. (2025). Role of battery energy storage systems: A comprehensive review on renewable energy zones integration in weak transmission networks. *Journal of Energy Storage, 128*, Article 117223. https://doi.org/10.1016/j.est.2025.117223

Salama, H. S., Ali, A., & Mahmoud, K. (2025). Adaptive control for microgrid frequency stability integrating battery energy storage and photovoltaic. *Scientific Reports, 15*(1), Article 43839. https://doi.org/10.1038/s41598-025-28321-x

Soares, L. T. F., Souza, A. C., Silva, W., Rezende, G. M. de, & Brandao, D. I. (2026). Battery energy storage system for grid frequency support using the virtual synchronous machine strategy. *Energies, 19*(13), Article 3015. https://doi.org/10.3390/en19133015

Syahbani, M. A., Ramli, M. A. M., Megantoro, P., Ardiansyah, A., Cahyani, I. D., Dinata, N. F. P., Firmansyah, R., Zohri, M., & Budiman, F. N. (2025). Performance enhancement of grid-forming inverter-controlled PV systems: A comparative study with and without battery energy storage under intermittent and unbalanced load conditions. *Results in Engineering, 27*, Article 105980. https://doi.org/10.1016/j.rineng.2025.105980

Wan, P., Huang, M., Mou, J., Tao, L., Zhang, S., & Hu, Z. (2025). Voltage unbalance control strategy for local shading photovoltaic grid-connected system. *Energies, 18*(3), Article 554. https://doi.org/10.3390/en18030554

Zhao, C., Andersen, P. B., Træholt, C., & Hashemi, S. (2023). Grid-connected battery energy storage system: A review on application and integration. *Renewable and Sustainable Energy Reviews, 182*, Article 113400. https://doi.org/10.1016/j.rser.2023.113400